Inverse Janus design of two-dimensional Rashba semiconductors

Qikun Tian,[1] Puxuan Li,[1] Jinghui Wei,[1] Ziyu Xing,[1] Guangzhao Qin,[2,*] and Zhenzhen Qin[1,†]

[1]*International Laboratory for Quantum Functional Materials of Henan, and School of Physics and Microelectronics, Zhengzhou University, Zhengzhou 450001, People's Republic of China*

[2]*National Key Laboratory of Advanced Design and Manufacturing Technology for Vehicle, College of Mechanical and Vehicle Engineering, Hunan University, Changsha 410082, People's Republic of China*

(Received 28 June 2023; accepted 21 August 2023; published 14 September 2023)

The search for optimal Rashba semiconductors with large Rashba constants, strong electric field responses, and potential thermoelectric properties is pivotal for spin field-effect transistors (SFETs) and Rashba thermoelectric devices. Herein, we employ first-principles calculations to explore the intrinsic Rashba spin splitting in a series of two-dimensional (2D) XYZ_2 (X, Y = Si, Ge, Sn; $X \neq Y$; Z = P, As, Sb, Bi) monolayers via unnatural inverse Janus structural design. Instead of common Janus-type Rashba systems, the $SiSnSb_2$ and $GeSnSb_2$ monolayers within inverse Janus structures are first predicted as ideal Rashba systems with isolated spin-splitting bands near the Fermi level, and the Rashba constants α_R are calculated as 0.94 and 1.27 eV Å, respectively. More importantly, the Rashba effect in such $SiSnSb_2$ and $GeSnSb_2$ monolayers can be more efficiently modulated by the external electric field compared to the biaxial or uniaxial strain, especially with $GeSnSb_2$ monolayer exhibiting a strong electric field response rate of 1.34 eÅ^2, leading to a short channel length, $L = 64$ nm. Additionally, owing to the inapplicability of work function and potential energy in assessing built-in electric field (E_{in}) in inverse Janus $SiSnSb_2$ and $GeSnSb_2$ structures, we further propose an effective method to characterize E_{in} through a view of fundamental charge transfer to approximately quantize the α_R and its variation under an external electric field. Our work not only proposes the $GeSnSb_2$ monolayer acting as a promising multifunctional material for potential applications in SFETs and Rashba thermoelectric devices but also inspires future research to introduce Rashba spin splitting in 2D materials through inverse Janus design.

DOI: 10.1103/PhysRevB.108.115130

I. INTRODUCTION

With the emergence of spintronics [1], the search for materials with large spin-orbit coupling (SOC) effect has become crucial for spin devices. Rashba effect [2] induced by SOC coupled with broken inversion symmetry in certain materials stimulates a wide range of research interests [3,4] since it is closely associated with spintronics, such as spin Hall effect [5], spin-orbit torque [6], and topological insulators [7]. Particularly, the Rashba spin splitting can tune the polarized spins by external electric field [8], thus offering considerable potential for application in spin field-effect transistors (SFETs) [9]. To describe the Rashba effect, Bychkov and Rashba proposed the Bychkov-Rashba form, which is one of the spin-orbital Hamiltonian forms, $H_{SOC} = \alpha_R\ (\boldsymbol{\sigma} \times \boldsymbol{k}) \cdot z$ [10], where α_R stands for the Rashba constant, $\boldsymbol{\sigma}$ for the Pauli spin matrices, $\boldsymbol{k}$ for the momentum, and z for the electric field direction. A high Rashba constant and strong electric field response rate are the keys to reduce the spin channel length and preserve spin coherence of SFETs. On the other hand, Rashba effect is demonstrated to be in favor of the thermoelectric properties in bulk BiTeI system due to the unique spin-splitting band structure [11]. In our recent review [12] of Rashba spin splitting optimizing thermoelectric property, we propose that the search for intrinsic Rashba-type thermoelectric materials, or the introduction of a Rashba spin splitting in common thermoelectric materials, may be promising ways to globally optimize the thermoelectric performance. Hence, designing ideal Rashba materials derived from original thermoelectric materials and studying their responses of Rashba constants to the external electric field are intriguing.

As known, the Janus structure [13,14], characterized by two distinct nanoscale faces, is generally employed in the two-dimensional (2D) systems to achieve the Rashba effect due to the intrinsic symmetry breaking. Typically, 2D Janus materials can be engineered by substituting atoms to disrupt the symmetry in original symmetric systems. Designing Janus structures with two- and three-atom layers is straightforward, achieved by ensuring different atoms at both ends. The electronic structures and Rashba properties of two-atom layer buckled honeycomb Janus structures, such as BiSb [15,16], AlBi [15], and three-atom layer transition-metal dichalcogenide (TMD) Janus MXY (M = Mo, W; X, Y = S, Se, Te; $X \neq Y$) [17–20] have been extensively studied. For four atomic-layer systems (single atomic-layer replacement), it is common to design Janus structures by making the two end atoms different, as exemplified by the Janus structures M_2XY (M = Ga, In; X, Y = S, Se, Te; $X \neq Y$) [21,22] and XZ_2Y (X, Y = P, As, Sb, Bi; $X \neq Y$; Z = Si, Ge, Sn) [23–25]. Beyond the common Janus structural design, many efforts

*gzqin@hnu.edu.cn
†qzz@zzu.edu.cn

have been devoted to achieve the ideal Rashba spin splitting by constructing 2D van der Waals heterostructures [26,27], seeking intrinsic polar materials (such as 2D Polar Perovskites ABX_3 [28] ($A = Cs^+$, Rb^+; $B = Pb^{2+}$, Sn^{2+}; $X =$ Cl, Br, I) and $TlSnX_3$ [29] ($X =$ Cl, Br, I)) or other effective means. Inspired by the prevalent Janus structures and the multiple atomic layers of numerous 2D materials, we are devoted to searching for more structural design strategies to introduce Rashba spin splitting in this work, which is expected to expand the scope of searching ideal Rashba materials beyond the traditional framework of structural design.

Lately, the original four atomic-layer systems X_2Z_2 ($X =$ Si, Ge, Sn; $Z =$ P, As, Sb, Bi) have been theoretically predicated to be dynamically stable by Özdamar *et al.* [30]. Additionally, 2D monolayer SnSb featuring a honeycomb lattice structure and 2D monolayer GeAs nanosheets have been successfully synthesized experimentally [31,32], providing an example of experimental synthesis of other X_2Z_2 materials. Due to the symmetry of the original system X_2Z_2 with four atomic layers, it is possible to design Janus structures by various ways. The practice of making the two end atoms different to obtain Janus structures XZ_2Y is common [23–25]. Liu *et al.* [23,24] and Babaee Touski *et al.* [25] have studied the unique electronic properties of Janus materials XZ_2Y, including the Rashba effect and Lifshitz transition, while the thermoelectric potential of XZ_2Y materials are ignored. Actually, the original systems X_2Z_2 have been identified as a potential class of thermoelectric materials [33–35]. Therefore, given the great potential of the Rashba effect to optimize thermoelectric properties [12], it is necessary to explore stronger Rashba effect and even modulation based on the original thermoelectric systems X_2Z_2. Consequently, we anticipate exploring the original thermoelectric materials X_2Z_2 by structural design, which may facilitate achieving the ideal Rashba effect and enable the design of multifunctional materials suitable for applications in both SFETs and Rashba thermoelectric devices.

In the present work, we use first-principles calculations to investigate the structural stability, electronic structure, and intrinsic Rashba effect in a series of 2D XYZ_2 (X, $Y =$ Si, Ge, Sn; $X \neq Y$; $Z =$ P, As, Sb, Bi) monolayers within the inverse Janus structures (by substituting intermediate atoms from four atomic-layer X_2Z_2), then further explore the modulation of Rashba effect under external electric field and strain. Among these 12 kinds of inverse Janus structures, the $SiSnSb_2$ and $GeSnSb_2$ monolayers are predicted as ideal Rashba semiconductors ($\alpha_R = 0.94$ and 1.27 eV Å) with isolated spin-splitting bands near the Fermi level. To clarify the underlying mechanism of such two Rashba systems with inverse Janus structures, we introduce a simple approach based on fundamental charge-transfer analysis to characterize the hidden E_{in} for approximately quantizing the magnitude of α_R and further establish that total charge transfer (Q_{t0}) and intrinsic E_{in} characterized by charge-transfer difference between the two ends (Q_{d0}), jointly dictate the Rashba constant variations under external electric field. Compared to strain modulation, the Rashba effect in $SiSnSb_2$ and $GeSnSb_2$ monolayers can be more efficiently modulated by external electric field, especially with $GeSnSb_2$ monolayer exhibiting a strong electric field response rate of 1.34 eÅ^2, leading to a short channel length $L = 64$ nm, thereby manifesting as a promising multifunctional material for SFETs and Rashba thermoelectric devices. In particular, our work could largely inspire future research to introduce Rashba spin splitting in other 2D materials through inverse Janus design.

II. COMPUTATIONAL METHODS

First-principles calculations were performed by using the Vienna *Ab initio* Simulation Package (VASP), which employs density-functional theory and the projected-augmented wave method [36,37]. The Perdew-Burke-Ernzerhof (PBE) exchange-correlation functional within the generalized gradient approximation was utilized [38]. To investigate the Rashba effect, our electronic band structure calculations were performed both with and without SOC. The kinetic energy cutoff for the plane-wave basis was set to be 620 eV. We relaxed all atoms to ensure an energy convergence of 10^{-6} eV and forcing convergence of 10^{-4} eV/Å. We used a 12 × 12 × 1 Gamma-point centered grid to sample the Brillouin zone (BZ). The ∼ 25 Å vacuum layer was included along the z axis to eliminate interactions between adjacent slabs. Additionally, the Heyd-Scuseria-Ernzerhof hybrid functional (HSE06) was also used to correct the electronic band structure [39,40]. The dynamical stability of inverse Janus XYZ_2 monolayers was checked via phonon-dispersion calculations with a large supercell 5 × 5 × 1 as implemented in the PHONOPY code [41]. Moreover, we tested the thermal stability of the inverse Janus XYZ_2 monolayers by performing *ab initio* molecular dynamics (AIMD) simulations at room temperature for 10 ps with a step of 2 fs. The Bader techniques were used to analyze the charge transfer [42]. The constant-energy contour plots of the spin texture were calculated using the PYPROCAR code [43].

III. RESULTS AND DISCUSSION

The X_2Z_2 systems exhibit D_{3h} symmetry with mirror symmetry, whereas inverse Janus XYZ_2 monolayers, formed by substituting an intermediate X atom in X_2Z_2 monolayers with a Y atom, disrupt mirror symmetry and possess a $P3m1(C_{3V})$ space group. The XYZ_2 monolayers feature a hexagonal lattice comprising covalently bonded four atomic layers with the same Z atoms at both ends and different X, Y atoms sandwiched, as illustrated in Fig. 1(a). The optimized lattice parameters of the XYZ_2 monolayers are summarized in Table I. Our calculated results demonstrate that the lattice constants of XYZ_2 monolayers increase with the growth of the atomic number of Z atoms, from P to Bi. Furthermore, the bond length of X and Y atoms l_{X-Y} and lattice constants increase in order of sandwiched Si-Ge, Si-Sn, and Ge-Sn when the two terminal atoms are kept. Thus, $GeSnBi_2$ has the maximum lattice constant value of 4.38 Å, while $SiGeP_2$ has the minimum lattice constant value of 3.59 Å. The bond-angle sum of θ_1 (θ_2) and θ_3 (θ_4) for all XYZ_2 monolayers is approximately 161°.

The cohesive energy E_{coh} of inverse Janus XYZ_2 monolayers is calculated by the following formula:

$$E_{coh} = [(n_1E_X + n_2E_Y + n_3E_Z) - E_{tot}]/(n_1 + n_2 + n_3). \quad (1)$$

TABLE I. Optimized lattice parameters of inverse Janus XYZ_2 monolayers: lattice constant $a = b$, bond length of X and Y atoms l_{X-Y}, vertical distance of X and Z atoms d_{X-Z}, vertical distance of Y and Z atoms d_{Y-Z}, bond angle of Z, X, and Y atoms θ_1, bond angle of Z, Y, and X atoms θ_2, bond angle of X, Z, and X atoms θ_3, bond angle of Y, Z, and Y atoms θ_4. Calculated cohesive energy and band gap without and with SOC using PBE method: E_{coh}, E_{g-PBE}, and $E_{g-PBE+SOC}$.

	$a = b$(Å)	l_{X-Y}(Å)	d_{X-Z}(Å)	d_{Y-Z}(Å)	θ_1(deg)	θ_2(deg)	θ_3(deg)	θ_4(deg)	E_{coh} (eV/atom)	E_{g-PBE}(eV)	$E_{g-PBE+SOC}$(eV)
$SiGeP_2$	3.59	2.43	0.99	1.09	103.47	104.77	57.37	56.87	3.89	1.49	1.46
$SiSnP_2$	3.73	2.63	0.96	1.26	102.51	106.34	57.72	56.21	3.63	0.69	0.62
$GeSnP_2$	3.80	2.70	1.03	1.23	103.19	105.62	57.48	56.52	3.40	1.07	1.01
$SiGeAs_2$	3.75	2.42	1.08	1.17	104.06	105.11	57.15	56.73	3.60	1.38	1.26
$SiSnAs_2$	3.88	2.62	1.05	1.33	103.22	106.52	57.47	56.13	3.39	0.53	0.40
$GeSnAs_2$	3.95	2.69	1.11	1.30	103.69	105.89	57.29	56.40	3.19	0.55	0.41
$SiGeSb_2$	4.06	2.42	1.21	1.28	104.44	105.24	57.00	56.68	3.31	0.85	0.64
$SiSnSb_2$	4.19	2.62	1.16	1.43	103.59	106.55	57.33	56.11	3.13	0.34	0.11
$GeSnSb_2$	4.25	2.68	1.21	1.41	103.90	106.03	57.21	56.34	2.98	0.31	0.07
$SiGeBi_2$	4.20	2.41	1.26	1.32	104.50	105.20	56.98	56.69	3.14	0.41	0
$SiSnBi_2$	4.33	2.61	1.21	1.48	103.60	106.53	57.32	56.12	2.98	0	0
$GeSnBi_2$	4.38	2.67	1.25	1.46	103.84	106.05	57.23	56.33	2.84	0	0

In Eq. (1), E_X, E_Y, and E_Z are the isolated atom energies of the elements X, Y, and Z, respectively; E_{tot} represents the total energy of the inverse Janus XYZ_2 monolayers; n_1, n_2, and n_3 denote the number of X, Y, and Z atoms in the unit cell, respectively. Our calculated results show that all inverse Janus XYZ_2 monolayers are energetically stable, as listed in Table I. Moreover, the phonon spectra and AIMD simulations at 300 K of $SiGeSb_2$, $SiSnSb_2$ and $GeSnSb_2$ monolayers are calculated to verify their dynamical and thermal stabilities as plotted in Figs. 1(c) and 1(d), and the nine phonon spectra and AIMD simulations at 300 K of other XYZ_2 monolayers are also depicted in Figs. S1 and S2 of the Supplemental Material [44], where no imaginary frequency is found for all the XYZ_2 structures and their free energy fluctuates in a narrow range, with no significant distortion of the equilibrium structure or bond breaking, indicating that they are dynamically and thermally stable.

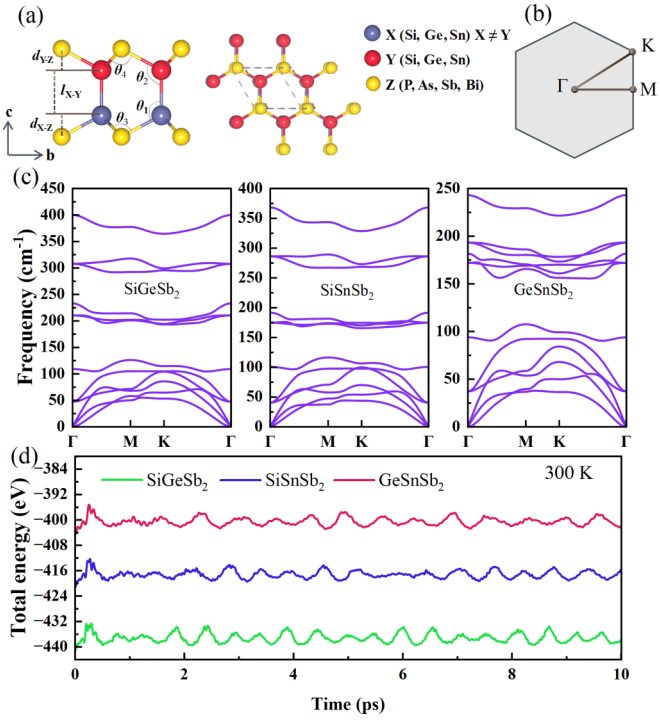

FIG. 1. (a) Side and top views of honeycomb crystal structure of XYZ_2 monolayers. Blue, red, and yellow balls denote X, Y, and Z atoms, respectively. (b) First Brillouin zone labeled with high-symmetry points. (c) Phonon spectra and (d) AIMD simulations of total energy fluctuation under 10 ps at 300 K of $SiGeSb_2$, $SiSnSb_2$, and $GeSnSb_2$ monolayers.

The electronic band structures of inverse Janus $SiSnSb_2$ and $GeSnSb_2$ monolayers are calculated employing PBE functional without and with SOC as shown in Fig. 2, while the band structures of other inverse Janus XYZ_2 monolayers are given in Fig. S3 [44]. In the absence of SOC, our results reveal that all inverse Janus XYZ_2 monolayers exhibit a band gap, with the exception of the $SiSnBi_2$ and $GeSnBi_2$ monolayers. Especially, the $SiGeP_2$, $SiSnP_2$, $GeSnP_2$, $SiGeAs_2$, and $SiGeSb_2$ monolayers are characterized as indirect band-gap semiconductors, whereas the $SiSnAs_2$, $GeSnAs_2$, $SiGeBi_2$, $SiSnSb_2$, and $GeSnSb_2$ monolayers display direct band-gap properties. When SOC is taken into account, the band-gap values for these monolayers are reduced. Interestingly, the $SiSnSb_2$ and $GeSnSb_2$ monolayers within unnatural inverse Janus structures, different from common Janus-type Rashba systems, both present the isolated spin-splitting bands near the Fermi level as ideal Rashba systems, as shown in Fig. 2. Thereby, the Rashba systems $SiSnSb_2$ and $GeSnSb_2$ are first proposed by utilizing an unnatural inverse Janus structural design strategy, providing a new perspective for future research to introduce Rashba spin splitting in other 2D thermoelectric materials. Next, we primarily focus on the analysis of $SiSnSb_2$ and $GeSnSb_2$ monolayers.

In the absence of SOC, the band-gap values of the $SiSnSb_2$ and $GeSnSb_2$ monolayers are 0.34 and 0.31 eV, respectively, and their valence-band maximum (VBM) and conduction-band minimum (CBM) points are both located at the Γ point. However, the primitive systems SiSb, GeSb, and SnSb are all indirect band-gap semiconductors [30], showing that by doping, the indirect band gap is transformed into direct band gap. Additionally, the hybrid functional HSE06 [39,40] is

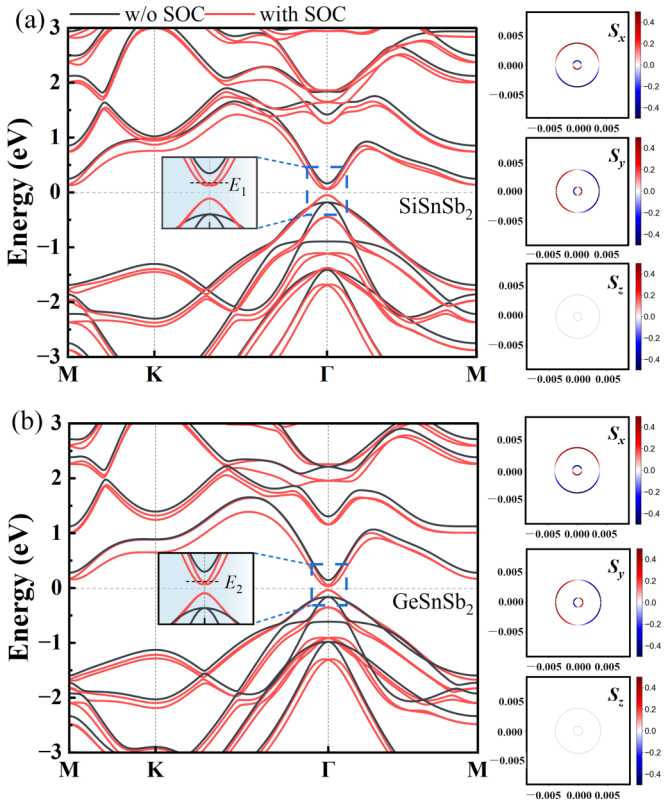

FIG. 2. Band structures of (a) $SiSnSb_2$ and (b) $GeSnSb_2$ monolayers. Black and red solid lines indicate methods of PBE and PBE+SOC, respectively. Enlarged view of Rashba spin-splitting bands at CBM near Fermi level is plotted in blue. Right parts represent 2D contour plots of spin textures for $SiSnSb_2$ and $GeSnSb_2$ monolayers at constant energy E_1 ($E_f + 0.07$ eV), E_2 ($E_f + 0.05$ eV) in $k_x - k_y$ plane centered at Γ point. Red color represents spin-up states and blue represents spin-down states. Projections of spin components S_x, S_y, and S_z are plotted.

also used to obtain more accurate band structures since PBE calculations are considered to underestimate the band gap [45] (as shown in Fig. S4 [44]), where the corrected band-gap values of the $SiSnSb_2$ and $GeSnSb_2$ monolayers are 0.91 and 0.84 eV, respectively. With the SOC included, the $SiSnSb_2$ and $GeSnSb_2$ monolayers possess band gaps of 0.11(0.64) and 0.07(0.58) eV by using the PBE-SOC (HSE-SOC) method, respectively. Then, the orbital components at both the VBM and CBM are calculated, as depicted in Fig. S5 [44]. The VBM is located at the Γ point and CBM is near the Γ point in the irreducible BZ, where the VBM is dominated by the $p_{x,y}$ orbital of the Sb atoms for both $SiSnSb_2$ and $GeSnSb_2$. The CBM is mainly contributed by the s orbital of the Si/Ge atoms and the p_z orbital of the Sb atoms for $SiSnSb_2$ and $GeSnSb_2$, resulting in the large Rashba effect. To quantify the strength of the Rashba effect, we calculated the Rashba constant α_R for $SiSnSb_2$ and $GeSnSb_2$ monolayers by $\alpha_R = 2E_R/k_R$ based on the results of PBE-SOC, where the E_R is Rashba energy and k_R is momentum offset. The calculated E_R, k_R, and α_R are 5.45 meV, 0.00858 Å^{-1}, and 1.27 eV Å for $GeSnSb_2$ monolayer and 4.11 meV, 0.0087 Å^{-1}, and 0.94 eV Å for $SiSnSb_2$ monolayer, respectively. Notice the α_R for $SiSnSb_2$ and $GeSnSb_2$ is a large value among some 2D materials, such as BiSb (2.3 eV Å) [16], WSeTe (0.52 eV Å) [17], and AlBi (2.77 eV Å) [15]. Since a large Rashba constant plays a role in reducing the spin channel length, the $GeSnSb_2$ monolayer could serve as the potential candidate for SFETs.

The 2D contour plots of spin textures for $SiSnSb_2$ and $GeSnSb_2$ monolayers are depicted at constant energy in the $k_x - k_y$ plane centered at the Γ point, where the Rashba spin-splitting bands consist of spin up (red color) and spin down (blue color). The concentric spin texture circles are the result of Rashba spin splitting near the CBM. Furthermore, the projections of the spin components S_x, S_y, and S_z are plotted, and we can see that only the *in-plane* S_x and S_y spin components are present in the Rashba splitting bands, while the *out-of-plane* S_z spin components are absent, indicating that the spin splitting of electrons in $SiSnSb_2$ and $GeSnSb_2$ monolayers is indeed purely 2D Rashba effect. Interestingly, Rashba spin-splitting bands with similar 2D pure Rashba nature are observed at energy points E_1 ($E_f + 0.07$ eV) for $SiSnSb_2$ monolayer and E_2 ($E_f + 0.05$ eV) for $GeSnSb_2$ monolayer.

Figures 3(a) and 3(b) depict the average electrostatic potential for SnSb, $SiSnSb_2$ and $GeSnSb_2$. The results show that the electrostatic potential-energy peaks of the primitive system SnSb are symmetric, consistent with the symmetric crystal structure, with four peak points, while for the $SiSnSb_2$ and $GeSnSb_2$ monolayers with broken structural symmetry, the electrostatic potential distributions are asymmetrical with three peaks at Sb_{bot} side, Sb_{top} side, and Sn position. Generally, the strength of intrinsic Rashba effect in common Janus structure is positively associated with its E_{in}, which could be reflected in the two aspects of work function and potential-energy difference [19,20,23,46]. However, from the two perspectives above, there is no obvious work function and potential-energy difference of Sb_{bot} side and Sb_{top} side for the two Rashba systems $SiSnSb_2$ and $GeSnSb_2$ since the elements at both ends of the crystal structure are identical, which is different to that of common Janus Rashba materials [18–20,23,46] with different atoms at both ends. To clarify the underlying mechanism of these two Rashba systems with such unique asymmetric structures, seeking an approach to determine the form of E_{in} arousing the intrinsic Rashba spin split is necessary. From the most basic perspective, the charge transfer is a key factor that determines the strength of E_{in} and even the magnitude of α_R which has been qualitatively demonstrated in typical common Janus structures [18,20]. For example, the α_R is found linearly correlated to the charge transfer between *X/Y* and *M* atoms in a series of 2D Janus TMDs [18]. Similarly, Zhou *et al.* demonstrated that the manipulation of Rashba effect in 1*T*-phase Janus monolayer WSSe through strain is completely governed by charge transfer and orbital components [20]. Assuming that charge transfer determines the intrinsic electric field E_{in} and then the α_R, we propose a method to characterize the E_{in} of such inverse Janus structures based on following Bader charge analysis. Figure 3(c) shows the charge transfer between the atoms of the adjacent layer for SnSb, $SiSnSb_2$, and $GeSnSb_2$ systems. For the pure SnSb, the two end atoms gain the electrons ($-0.19\ e$, e_0^-) and the intermediate atoms lose the same electrons ($0.19\ e$, $-e_0^-$), leading to the reversed localized electric field (E_0) and absent E_{in}, as revealed in Fig. 3(d).

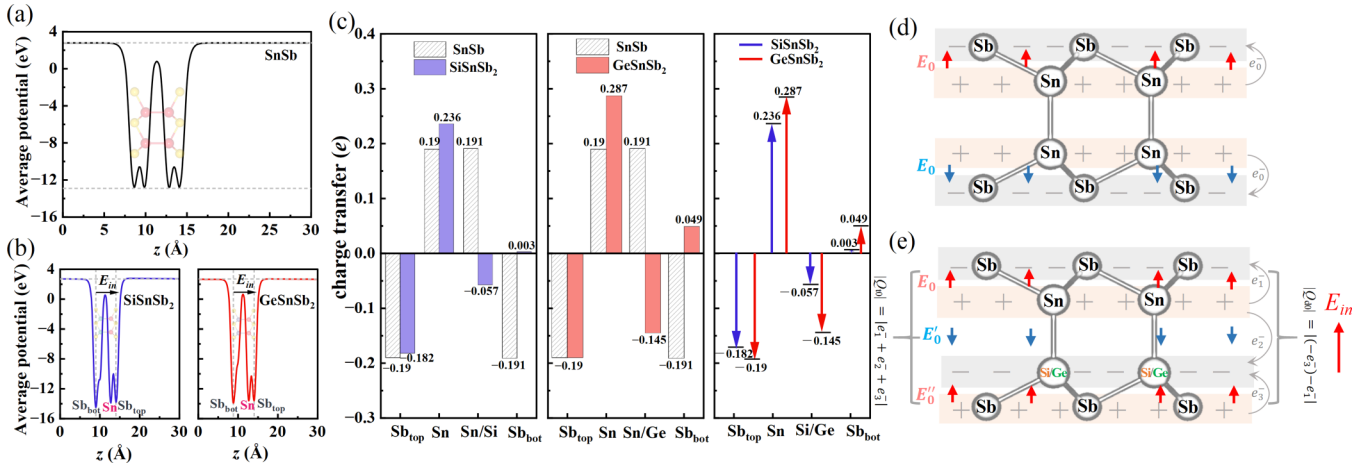

FIG. 3. Electrostatic potential of (a) SnSb, (b) $SiSnSb_2$, and $GeSnSb_2$ monolayers along z direction. (c) Comparative charge-transfer plots of SnSb and $SiSnSb_2$, SnSb and $GeSnSb_2$, and $SiSnSb_2$ and $GeSnSb_2$. (d), (e) Schematic diagram of charge transfer and E_{in} of SnSb, $SiSnSb_2$, and $GeSnSb_2$ monolayers. E_0, $E_0^{'}$, $E_0^{''}$ represent localized electric field. $|Q_{d0}|$: $|(-e_3^-) - e_1^-|$, $|Q_{t0}|$: $|e_1^- + e_2^- + e_3^-|$. e_1^-, e_2^-, e_3^- represent gaining electrons with negative value and $-e_1^-$, $-e_2^-$, $-e_3^-$ represent losing electrons with positive value.

Nevertheless, for $SiSnSb_2$ and $GeSnSb_2$ with inverse Janus structure, it is found that despite the fact that the two end elements have the same electronegativity, their charge transfer behave differently, with the Sb_{top} side of $SiSnSb_2$ ($GeSnSb_2$) monolayers gaining electrons of -0.182 e (-0.19 e, e_1^-) and the Sb_{bot} side losing electrons of 0.003 e (0.049 e, $-e_3^-$), respectively, as illustrated in Fig. 3(e), where the charge-transfer difference between the two ends ($|Q_{d0}|$, $|(-e_3^-) - e_1^-|$) creates a potential gradient in the base plane, resulting in an E_{in} between the topmost and lowest layers. More specifically, the intermediate sublayers of $SiSnSb_2$ ($GeSnSb_2$) monolayers could exhibit localized electric field (E_0, $E_0^{'}$, $E_0^{''}$), due to the Si/Ge sublayer gaining electrons of -0.057 e (-0.145 e, $e_2^- + e_3^-$) and the Sn sublayer losing electrons of 0.236 e (0.287 e, $-(e_1^- + e_2^-)$). By further examining the Rashba constant α_R and inner charge-transfer characterized intrinsic E_{in} for the two inverse Janus systems, we found the α_R of $GeSnSb_2$ (1.27 eV Å) is larger than that of $SiSnSb_2$ (0.94 eV Å), which is positively related to the $|Q_{d0}|$ (0.239 e and 0.185 e for $GeSnSb_2$ and $SiSnSb_2$ monolayers). The positive correlation reveals the intrinsic effects of charge transfer and E_{in} on the Rashba constant and subsequent manipulation trends under external electric field further validate the effectiveness. A larger value of $|Q_{d0}|$ indicates a greater probability of observing large Rashba constants in a class of Rashba materials with the similar structure. Interestingly, a positive correlation between the total charge transfer $|Q_{t0}|$ ($|e_1^- + e_2^- + e_3^-|$, 0.336 e, and 0.239 e for $GeSnSb_2$ and $SiSnSb_2$ monolayers) and the α_R is also discovered, which may play a role in affecting α_R under external electric field modulation. Our proposed relationship contributes to a more comprehensive understanding of the underlying mechanism governing the Rashba effect and provides a perspective for future research in Rashba systems, especially for inverse Janus Rashba systems.

As mentioned above, for the common Janus structures MXY (taking MoSSe as an example), the magnitude of E_{in} is generally estimated by dividing the difference in potential energy by the difference in distance from the atoms at the two ends to the origin due to the different electronegativity of the atoms at the two ends [19] [as shown in Fig. 4(a_1)]. However, due to the unique crystal structure and the same electronegativity of the atoms at the two ends of inverse Janus $SiSnSb_2$ and $GeSnSb_2$ materials without obvious work function and potential-energy difference, it may not be applicable to inverse Janus systems using the above traditional method. Considering the charge-transfer difference can create a potential gradient in the base plane, resulting in an intrinsic E_{in}, we utilize the $|Q_{d0}|$ ($|Q_{bot} - Q_{top}|$) to characterize the magnitude of E_{in} for the specific inverse Janus $SiSnSb_2$ and $GeSnSb_2$ structures [as also shown in Fig. 4(a_1)]. To further clarify the uniqueness of charge-transfer mechanism for inverse Janus structures relative to the non-Janus and common Janus structures, the diagrams of geometries with a full range of information about the charge transfer and localized electric field are drawn in the scope of such four atomic-layer systems (taking SnSb, XSn_2Y, $SiSnSb_2$ and $GeSnSb_2$ as examples), as illustrated in Fig. 4(a_2). Next, we investigate the changes of the electronic structures and Rashba spin splitting of $SiSnSb_2$ and $GeSnSb_2$ under the action of external electric field, as shown in Fig. S6 [44] and Fig. S9(d) [44], where the applied external electric field ranges from -0.2 to 0.2 V Å^{-1}, which is available for experimental size of electric field (0.3 V Å^{-1}) [47]. Due to the $|Q_{t0}|$ and $|Q_{d0}|$ both exhibiting a positive correlation with α_R in original systems, we predict that the variation of $|Q_{t0}|$ and $|Q_{d0}|$ under external electric field is the key factor influencing the variation of α_R under external electric field and the relation is schematically displayed in Fig. 4(a_3). Moreover, we further study the effect of charge doping on the electronic structures, charge transfer, and electrostatic potential of the two Rashba $SiSnSb_2$ and $GeSnSb_2$ monolayers with the doping range from -0.4 e to 0.4 e, as shown in Fig. S7 of the Supplemental Material [44]. The charge doping could greatly change the location of Fermi level and even induce the semiconductor-to-metallic phase transition. Thus, the charge doping limits the effective regulation of key parameters required in Rashba semiconductors to some extent. Additionally, the effect of strain (uniaxial, biaxial) on the band structures and the Rashba effect of inverse Janus

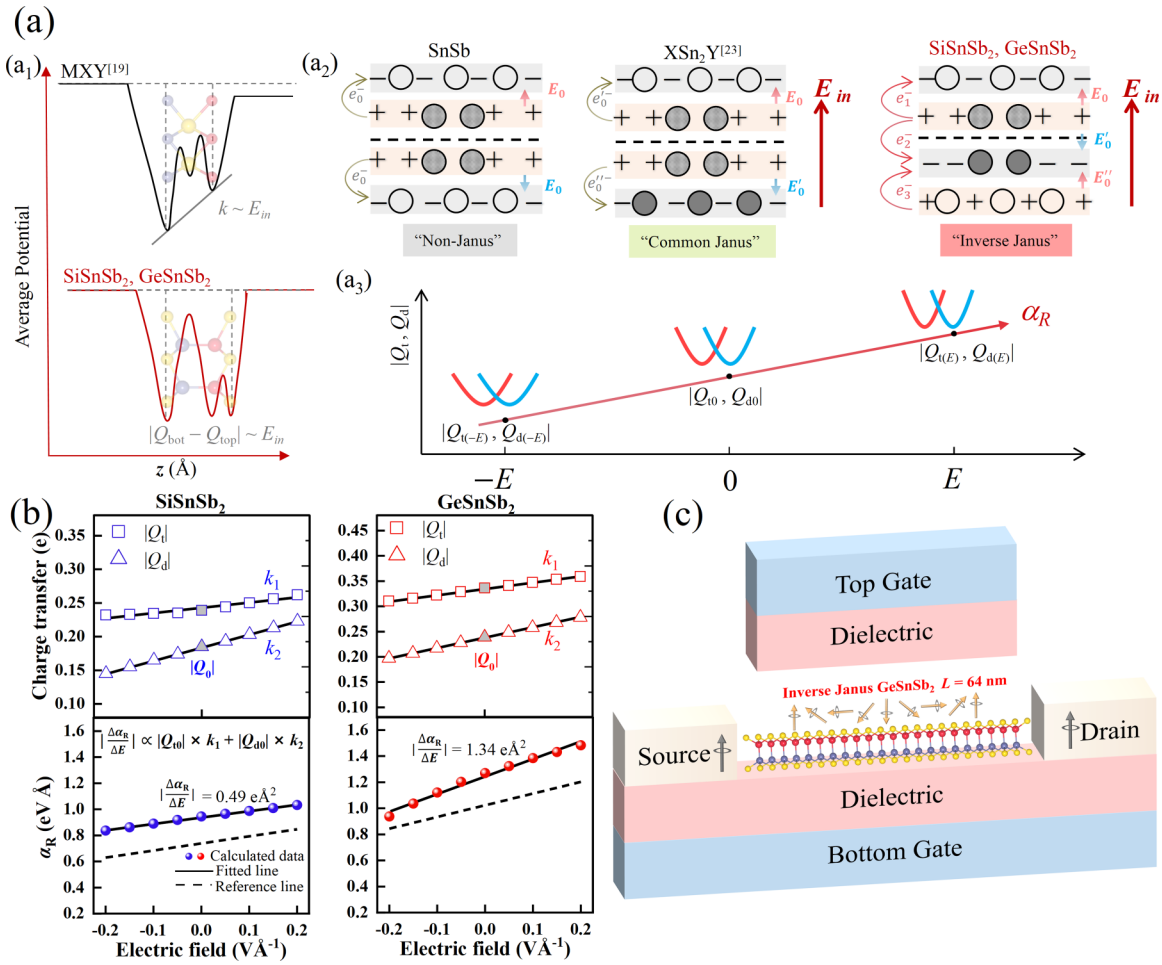

FIG. 4. (a_1) Schematic diagrams of electrostatic potential of *MXY* (taking MoSSe [19] as example), $SiSnSb_2$, and $GeSnSb_2$. (a_2) Schematic diagrams of structure, charge transfer, E_0, $E_0^{'}$, $E_0^{''}$, and E_{in} of non-Janus SnSb monolayer, common Janus XSn_2Y monolayer [23] (E_{in} as example of $SbSn_2Bi$), and inverse Janus $SiSnSb_2$ and $GeSnSb_2$. (a_3) Schematic diagrams of variation of $|Q_t|$, $|Q_d|$, and Rashba effect under external electric field E. (b) Electric field dependence of charge transfer $|Q_t|$, $|Q_d|$, and Rashba constant α_R for inverse Janus $SiSnSb_2$ and $GeSnSb_2$ monolayers. Solid and dashed lines represent slope of fit based on calculated data and Eq. (2). (c) Schematic diagram of SFET based on inverse Janus structures $SiSnSb_2$ and $GeSnSb_2$ (taking $GeSnSb_2$ as example). Spin precession between source and drain can be governed by gate voltage.

structures $SiSnSb_2$ and $GeSnSb_2$ is also studied (as shown in Figs. S8 and S9 [44]). (Detailed discussion is included in the Supplemental Material [44].) The results demonstrate that the Rashba effect in $SiSnSb_2$ and $GeSnSb_2$ monolayers can be more efficiently modulated by the external electric field compared to strain modulation; thus, we then focus on the relationship between charge transfer and Rashba constant response to the external electric field.

Figure 4(b) displays the response of $|Q_t|$, $|Q_d|$, and α_R to the applied external electric field, where $|Q_t|$, $|Q_d|$, and α_R exhibit a positive linear trend. The response of α_R to the applied external electric field is described by the value of the linear fitting slope, $\frac{\Delta\alpha_R}{\Delta E}$. Similarly, the response of $|Q_t|$, $|Q_d|$ to the applied external electric field can be defined as $\frac{\Delta Q_t}{\Delta E}$ and $\frac{\Delta Q_d}{\Delta E}$, respectively. To explain the distinct $\frac{\Delta\alpha_R}{\Delta E}$ for $GeSnSb_2$ and $SiSnSb_2$ monolayers, we introduce a mathematical expression:

$$\frac{\Delta\alpha_R}{\Delta E} \propto |Q_{t0}| \times k_1 + |Q_{d0}| \times k_2. \quad (2)$$

In Eq. (2), k_1 and k_2 denote $\frac{\Delta Q_t}{\Delta E}$ and $\frac{\Delta Q_d}{\Delta E}$. Especially, the $|Q_{t0}|$ and $|Q_{d0}|$ of $GeSnSb_2$ ($SiSnSb_2$) monolayers are 0.336 and 0.239 e (0.239 and 0.185 e), respectively. The values of $\frac{\Delta Q_t}{\Delta E}$ and $\frac{\Delta Q_d}{\Delta E}$ are $+0.123$ and $+0.203\,\mathrm{eV^{-1}}$ Å ($+0.077$ and $+0.194\,\mathrm{eV^{-1}}$ Å) for $GeSnSb_2$ ($SiSnSb_2$) monolayer, respectively. As a result, the numerical values on the right side of Eq. (2) are 0.090 and 0.054 for $GeSnSb_2$ and $SiSnSb_2$ monolayers. We can predict that the direction of the Rashba constant electric field response rate of $GeSnSb_2$ and $SiSnSb_2$ monolayers is positive and the value of Rashba constant electric field response rate of $GeSnSb_2$ is larger than $SiSnSb_2$, which are in agreement with the real values of $\frac{\Delta\alpha_R}{\Delta E} = +1.34$ ($+0.49\,\mathrm{eÅ^2}$) for $GeSnSb_2$ ($SiSnSb_2$) monolayers. This expression reveals that the Q_{t0} and the intrinsic E_{in}, characterized by Q_{d0}, collectively govern the response of Rashba constant to the external electric field. From the perspective of underlying physical mechanism, as $|Q_{t0}|$ represents the total charge transfer and $|Q_{d0}|$ signifies the charge-transfer difference between the both ends, a uniform

change in external electric field strength results in a uniform variation in $|Q_{t0}|$ and $|Q_{d0}|$, thereby exhibiting a similar trend for both $\frac{\Delta Q_t}{\Delta E}$ and $\frac{\Delta Q_d}{\Delta E}$ in $SiSnSb_2$ and $GeSnSb_2$; however, the behavior of $\frac{\Delta\alpha_R}{\Delta E}$ in $SiSnSb_2$ and $GeSnSb_2$ is different, where the Rashba constant increases more rapidly for the $GeSnSb_2$ monolayer compared to the $SiSnSb_2$ monolayer under external electric field; thus, we propose quantifying the electric field response strength of charge transfer by multiplying $\frac{\Delta Q_t}{\Delta E}$ with $|Q_{t0}|$ and $\frac{\Delta Q_d}{\Delta E}$ with $|Q_{d0}|$. The larger $|Q_{t0}| \times \frac{\Delta Q_t}{\Delta E} + |Q_{d0}| \times \frac{\Delta Q_d}{\Delta E}$ results in the larger $\frac{\Delta\alpha_R}{\Delta E}$ in $GeSnSb_2$ monolayer. Our proposed Eq. (2) based on fundamental charge-transfer analysis provides a quantitative understanding of the direction and velocity of the electric field response, which may guide the selection of the inverse Janus Rashba materials with the largest Rashba constant response velocity under electric field modulation.

The absolute value of Rashba constant electric field response rate $|\frac{\Delta\alpha_R}{\Delta E}|$ is important to the application of SFETs [15]. Utilizing the Rashba effect, Datta and Das first proposed the idea of SFETs in 1990 [9], and a number of spin devices were subsequently proposed and designed based on channel length [8,48–53]. Maintaining spin coherence is a significant obstacle in the development of spin devices. To preserve spin coherence, the solution is seeking materials with high Rashba constants and strong electric field response to reduce the spin channel length. Compared to previously typical 2D Rashba systems BiSb [15] (0.92 eÅ^2), AlBi [15] (0.047 eÅ^2), $T-RbPbBr_3$ [28] (0.177 eÅ^2), $T-RbPbI_3$ [28] (0.544 eÅ^2), $TlSnBr_3$ [29] (0.23 eÅ^2) and $TlSnI_3$ [29] (0.79 eÅ^2), the $GeSnSb_2$ monolayer has the largest response rate $|\frac{\Delta\alpha_R}{\Delta E}|$ with the magnitude of 1.34 eÅ^2 and the $SiSnSb_2$ monolayer has a relatively large value of 0.49 eÅ^2 among these 2D materials. Hence, we propose a SFET device based on inverse Janus structures $SiSnSb_2$ and $GeSnSb_2$ with large Rashba constants and strong electric field response rates, as shown in Fig. 4(c). We can see that the source and drain of the SFETs are made of ferromagnetic materials that have the same spin polarizations along the $+z$ direction and the spin channel is quasi-1D along the x direction. Rashba effect could influence the behavior of electron spins, the precession angle $\theta = 2\alpha_R m^* L/\hbar^2$ [15,28,29], in which m^* is electron effective mass and L is the length between source and drain. The α_R can be modulated by changing the precession angle θ. To make the spin direction of the electrons arriving at the drain opposite to the source, $\Delta\theta$ should be greater than π, which can be accomplished by applying electric field to tune α_R, so the channel length is $L = \pi\hbar^2/2\Delta\alpha_R m^*$ [15,28,29]. The estimated gate voltage ranges between −5 and 5 V, with top and bottom gates close to 50 Å apart, implying that the electric field varies between −0.1 and 0.1 V Å. Thus, the values of $\Delta\alpha_R$ are 0.098 and 0.265 eV Å for $SiSnSb_2$ and $GeSnSb_2$. Moreover, the values of m^* of $SiSnSb_2$ and $GeSnSb_2$ are $\hbar^2 k_R^2/2E_R \approx 0.09$ and $0.07\, m_e$. We can obtain the quantitative estimations of L as about 135 and 64 nm for $SiSnSb_2$ and $GeSnSb_2$, respectively. Compared to the channel length of other primitive systems for SFETs, such as BiSb [15] ($L = 158$ nm), $T-RbPbBr_3$ [28] ($L = 172$ nm), $T-RbPbI_3$ [28] ($L = 72$ nm), $TlSnBr_3$ [29]($L = 220$ nm), and $TlSnI_3$ [29]($L = 102$ nm), our designed SFETs based on inverse Janus structures $SiSnSb_2$ and $GeSnSb_2$ have short spin channel lengths, particularly the $GeSnSb_2$ with minimal value ($L = 64$ nm). Thus, the $SiSnSb_2$ and $GeSnSb_2$ monolayers with large Rashba constants and strong electric field response rates could serve as promising candidates for SFETs.

It is worth noting that Huang *et al.* theoretically reported the *n*-type SiSb monolayer has the good thermoelectric property with a $ZT \sim 2$ at 700 K [33] and Lou *et al.* also theoretically explored *p*-type α-GeSb monolayer with an ultralow thermal conductivity of 0.19 W/mK with a $ZT \sim 1.2$ at room temperature [35]. Thus, the successful introduction of a Rashba spin splitting in the $SiSnSb_2$ and $GeSnSb_2$ monolayers is promising to further optimize the thermoelectric performance based on the original thermoelectric system SiSb and GeSb, making them potential Rashba-type thermoelectric materials.

Before closing, we would like to discuss the experimental feasibility of synthesizing the class of inverse Janus structures. Recently, 2D common Janus structures have been successfully synthesized in experiment. For instance, the typical 2D Janus MoSSe monolayer was produced by replacing the top-layer S with Se atoms based on MoS_2 structure [54] or replacing the Se atomic layer of the $MoSe_2$ structure with S atoms [55], demonstrating the feasibility of 2D Janus structures' experimental realization. Notably, Kandemir *et al.* checked the experimental realization based on the total-energy difference Δ between the final energy of Janus structure and initial energy of symmetric InSe/InS monolayer, which indicated that the transformation from InSe to In_2SSe was favorable ($\Delta < 0$) and showed exothermic formation energy, whereas InS to InSSe was not favorable [56]. Similarly, we further checked the Δ between the final energy of inverse Janus XYZ_2 monolayers and initial energy of X_2Z_2 monolayers to check the feasibility of synthesizing of the inverse Janus XYZ_2 monolayers. It was found that the transformation from SnSb to the inverse Janus $SiSnSb_2$ ($GeSnSb_2$) structure was favorable ($\Delta < 0$) and exhibited exothermic formation energy, whereas SiSb to $SiSnSb_2$ (GeSb to $GeSnSb_2$) was not favorable ($\Delta > 0$) and requires energy to form the $SiSnSb_2$ ($GeSnSb_2$) structure. Thus, by substituting Sn layer from SnSb was found to be an easy route to achieve the inverse Janus $SiSnSb_2$ and $GeSnSb_2$ structures. Actually, 2D Sb monolayer featuring a honeycomb lattice structure with two atomic layers has been successfully synthesized experimentally [57]. Therefore, there is potential to expect the experimental synthesis of Janus SbX monolayer with two different atomic layers, such as SbSn and SbSi monolayer, by replacing Sb layer on one side with Si or Sn layer. Assuming the successful experimental synthesis of Janus SbX monolayer, it is possible to bond the two Janus SbSn and SbSi monolayers in the Sb-Sn-Si-Sb order, which might constitute the inverse Janus $SiSnSb_2$ with four atomic layers. Notably, the Cu_2MX_4 (M = Mo, W; X = S, Se) nanosheets consisting of different internal M and Cu atoms have been successfully synthesized in experiment by a solvothermal method [58,59]. Although it is a challenge to change the internal atoms chemically in experiment, we look forward to realizing the designed inverse Janus XYZ_2 structures in the future in consideration of theoretical prediction and experimental synthesis of similar structures.

IV. CONCLUSION

In this work, we employed first-principles calculations to explore the intrinsic Rashba spin splitting in a series of 2D inverse Janus XYZ_2 monolayers. Our phonon spectra and AIMD simulations revealed that the series of inverse Janus XYZ_2 monolayers are dynamically and thermally stable, indicating their potential for experimental synthesis. Notably, the Rashba effect was first introduced into both $SiSnSb_2$ and $GeSnSb_2$ monolayers ($\alpha_R = 0.94$ and $1.27\,eV\,Å$) via unnatural inverse Janus design by replacing the inner atom layer, unlike other Rashba systems based on the conventional Janus structure with different atoms at both ends. Moreover, the underlying mechanism influencing the strength of the Rashba effect for inverse Janus $SiSnSb_2$ and $GeSnSb_2$ monolayers was revealed by utilizing the electrostatic potential energy and charge transfer. Generally, there is a positive correlation between the Rashba constant and built-in electric field, but due to the inapplicability of work function and potential energy in assessing E_{in} in inverse Janus $SiSnSb_2$ and $GeSnSb_2$ structures, we proposed a method to characterize E_{in} through a view of fundamental charge transfer to approximately quantize the α_R. The impact of external electric field and strain on the band structures and the Rashba effect of $SiSnSb_2$ and $GeSnSb_2$ monolayers was also investigated. Compared to strain modulation, the Rashba effect in $SiSnSb_2$ and $GeSnSb_2$ monolayers can be more efficiently modulated by the external electric field. Furthermore, by examining charge transfer in these two inverse Janus Rashba systems under varying electric field strengths, we established that both the Q_{t0} and the intrinsic E_{in}, characterized by Q_{d0}, collectively govern Rashba constant variations under external electric field. Notably, the $GeSnSb_2$ monolayer exhibited a strong electric field response rate of $1.34\,eÅ^2$, which is a very large value among the 2D materials found so far, resulting in a short channel length $L = 64\,nm$, therefore making it a promising candidate for multifunctional materials in SFETs and Rashba thermoelectric devices.

ACKNOWLEDGMENTS

Z.Q. is supported by the National Natural Science Foundation of China (Grants No. 12274374 and No. 11904324) and the China Postdoctoral Science Foundation (Grant No. 2018M642774). G.Q. is supported by the National Natural Science Foundation of China (Grant No. 52006057), the Fundamental Research Funds for the Central Universities (Grants No. 531119200237 and No. 541109010001). The numerical calculations in this work are supported by National Supercomputing Center in Zhengzhou.

Z.Q. conceived and designed the research; Q.T. carried out the calculations and analyzed the calculated results; G.Q. participated in the discussion and provided insightful suggestions; and all the authors contributed to the final revision of this paper.

The authors declare no competing interests.

[1] I. Žutić, J. Fabian, and S. D. Sarma, Spintronics: Fundamentals and applications, Rev. Mod. Phys. **76**, 323 (2004).

[2] E. Rashba, Properties of semiconductors with an extremum loop. 1. Cyclotron and combinational resonance in a magnetic field perpendicular to the plane of the loop, Sov. Phys. Solid State **2**, 1109 (1960).

[3] A. Manchon, H. C. Koo, J. Nitta, S. M. Frolov, and R. A. Duine, New perspectives for Rashba spin–orbit coupling, Nat. Mater. **14**, 871 (2015).

[4] G. Bihlmayer, P. Noël, D. V. Vyalikh, E. V. Chulkov, and A. Manchon, Rashba-like physics in condensed matter, Nat. Rev. Phys. **4**, 642 (2022).

[5] J. Sinova, D. Culcer, Q. Niu, N. A. Sinitsyn, T. Jungwirth, and A. H. MacDonald, Universal Intrinsic Spin Hall Effect, Phys. Rev. Lett. **92**, 126603 (2004).

[6] I. Mihai Miron, G. Gaudin, S. Auffret, B. Rodmacq, A. Schuhl, S. Pizzini, J. Vogel, and P. Gambardella, Current-driven spin torque induced by the Rashba effect in a ferromagnetic metal layer, Nat. Mater. **9**, 230 (2010).

[7] M. Z. Hasan and C. L. Kane, Colloquium : Topological insulators, Rev. Mod. Phys. **82**, 3045 (2010).

[8] M. Kepenekian, R. Robles, C. Katan, D. Sapori, L. Pedesseau, and J. Even, Rashba and Dresselhaus effects in hybrid organic–inorganic perovskites: From basics to devices, ACS Nano **9**, 11557 (2015).

[9] S. Datta and B. Das, Electronic analog of the electro-optic modulator, Appl. Phys. Lett. **56**, 665 (1990).

[10] Y. A. Bychkov and E. I. Rashba, Properties of a 2D electron gas with lifted spectral degeneracy, JETP Lett. **39**, 78 (1984).

[11] L. Wu, J. Yang, S. Wang, P. Wei, J. Yang, W. Zhang, and L. Chen, Two-dimensional thermoelectrics with Rashba spin-split bands in Bulk BiTeI, Phys. Rev. B **90**, 195210 (2014).

[12] Q. Tian, W. Zhang, Z. Qin, and G. Qin, Novel optimization perspectives for thermoelectric properties based on Rashba spin splitting: A mini review, Nanoscale **13**, 18032 (2021).

[13] M. Yagmurcukardes, Y. Qin, S. Ozen, M. Sayyad, F. M. Peeters, S. Tongay, and H. Sahin, Quantum properties and applications of 2D Janus crystals and their superlattices, Appl. Phys. Rev. **7**, 011311 (2020).

[14] L. Zhang, Z. Yang, T. Gong, R. Pan, H. Wang, Z. Guo, H. Zhang, and X. Fu, Recent advances in emerging Janus two-dimensional materials: From fundamental physics to device applications, J. Mater. Chem. A **8**, 8813 (2020).

[15] K. Wu, J. Chen, H. Ma, L. Wan, W. Hu, and J. Yang, Two-dimensional giant tunable Rashba semiconductors with two-atom-thick buckled honeycomb structure, Nano Lett. **21**, 740 (2021).

[16] S. Singh and A. H. Romero, Giant tunable Rashba spin splitting in a two-dimensional BiSb monolayer and in BiSb/AlN heterostructures, Phys. Rev. B **95**, 165444 (2017).

[17] T. Hu, F. Jia, G. Zhao, J. Wu, A. Stroppa, and W. Ren, Intrinsic and anisotropic Rashba spin splitting in Janus transition-metal dichalcogenide monolayers, Phys. Rev. B **97**, 235404 (2018).

[18] J. Chen, K. Wu, H. Ma, W. Hu, and J. Yang, Tunable Rashba spin splitting in Janus transition-metal dichalcogenide monolayers via charge doping, RSC Adv. **10**, 6388 (2020).

[19] S.-B. Yu, M. Zhou, D. Zhang, and K. Chang, Spin Hall effect in the monolayer Janus compound MoSSe enhanced

by Rashba spin-orbit coupling, Phys. Rev. B **104**, 075435 (2021).

[20] W. Zhou, J. Chen, B. Zhang, H. Duan, and F. Ouyang, Manipulation of the Rashba spin-orbit coupling of a distorted 1 T-phase Janus WSSe monolayer: Dominant role of charge transfer and orbital components, Phys. Rev. B **103**, 195114 (2021).

[21] Y. Guo, S. Zhou, Y. Bai, and J. Zhao, Enhanced piezoelectric effect in Janus Group-III chalcogenide monolayers, Appl. Phys. Lett. **110**, 163102 (2017).

[22] T. V. Vu, V. T. T. Vi, C. V. Nguyen, H. V. Phuc, and N. N. Hieu, Computational prediction of electronic and optical properties of Janus Ga_2SeTem, J. Phys. D: Appl. Phys. **53**, 455302 (2020).

[23] M.-Y. Liu, L. Gong, Y. He, and C. Cao, Tuning Rashba effect, band inversion, and spin-charge conversion of Janus XSn_2Y monolayers via an external field, Phys. Rev. B **103**, 075421 (2021).

[24] M.-Y. Liu, L. Gong, Y. He, and C. Cao, Intraband Lifshitz transition and Stoner ferromagnetism in Janus P A_2As (A = Si, Ge, Sn, and Pb) monolayers, Phys. Rev. B **104**, 035409 (2021).

[25] S. Babaee Touski and N. Ghobadi, Structural, electrical, and Rashba properties of monolayer Janus Si_2 XY (X, Y = P, As, Sb, and Bi), Phys. Rev. B **103**, 165404 (2021).

[26] S. Gupta and B. I. Yakobson, What dictates Rashba splitting in 2D van der Waals heterobilayers, J. Am. Chem. Soc. **143**, 3503 (2021).

[27] N. Yu, J. Yuan, K. Li, and J. Wang, Tunable Rashba spin splitting in two-dimensional graphene/As-I heterostructures, Appl. Surface Sci. **427**, 10 (2018).

[28] J. Chen, K. Wu, W. Hu, and J. Yang, Tunable Rashba spin splitting in two-dimensional polar perovskites, J. Phys. Chem. Lett. **12**, 1932 (2021).

[29] Y. Jin, J. Li, G. Wang, Q. Zhang, Z. Liu, and X. Mao, Giant tunable Rashba spin splitting in two-dimensional polar perovskites $TlSnX_3$(X = Cl, Br, I), Phys. Chem. Chem. Phys. **24**, 17561 (2022).

[30] B. Özdamar, G. Özbal, M. N. Çınar, K. Sevim, G. Kurt, B. Kaya, and H. Sevinçli, Structural, vibrational, and electronic properties of single-layer hexagonal crystals of Group IV and V elements, Phys. Rev. B **98**, 045431 (2018).

[31] H. Li, D. Zhou, Q. He, N. Si, B. Xin, S. Bu, Q. Ji, H. Li, H. Fuchs, and T. Niu, Experimental realization and phase engineering of a two-dimensional SnSb Binary honeycomb lattice, ACS Nano **15**, 16335 (2021).

[32] C. S. Jung, D. Kim, S. Cha, Y. Myung, F. Shojaei, H. G. Abbas, J. A. Lee, E. H. Cha, J. Park, and H. S. Kang, Two-dimensional GeAs with a visible range band gap, J. Mater. Chem. A **6**, 9089 (2018).

[33] H. H. Huang, X. Fan, D. J. Singh, and W. T. Zheng, The thermal and thermoelectric transport properties of SiSb, GeSb and SnSb monolayers, J. Mater. Chem. C **7**, 10652 (2019).

[34] A. Bafekry, M. Yagmurcukardes, B. Akgenc, M. Ghergherehchi, and B. Mortazavi, First-principles investigation of electronic, mechanical and thermoelectric properties of graphene-like XBi (X = Si, Ge, Sn) monolayers, Phys. Chem. Chem. Phys. **23**, 12471 (2021).

[35] A. Lou, Q.-B. Liu, and H.-H. Fu, Enhanced thermoelectric performance by lone-pair electrons and bond anharmonicity in the two-dimensional Ge_2Y_2 family of materials with Y = N, P, As, or Sb, Phys. Rev. B **105**, 075431 (2022).

[36] G. Kresse and J. Furthmüller, Efficient iterative schemes for ab initio total-energy calculations using a plane-wave basis set, Phys. Rev. B **54**, 11169 (1996).

[37] P. E. Blöchl, Projector augmented-wave method, Phys. Rev. B **50**, 17953 (1994).

[38] J. P. Perdew, K. Burke, and M. Ernzerhof, Generalized Gradient Approximation Made Simple, Phys. Rev. Lett. **77**, 3865 (1996).

[39] J. Heyd, G. E. Scuseria, and M. Ernzerhof, Hybrid functionals based on a screened Coulomb potential, J. Chem. Phys. **118**, 8207 (2003).

[40] J. Heyd, G. E. Scuseria, and M. Ernzerhof, Erratum: "Hybrid functionals based on a screened Coulomb potential" [J. Chem. Phys. 118, 8207 (2003)], J. Chem. Phys. **124**, 219906 (2006).

[41] A. Togo and I. Tanaka, First principles phonon calculations in materials science, Scr. Mater. **108**, 1 (2015).

[42] W. Tang, E. Sanville, and G. Henkelman, A grid-based Bader analysis algorithm without lattice bias, J. Phys.: Condens. Matter **21**, 084204 (2009).

[43] U. Herath, P. Tavadze, X. He, E. Bousquet, S. Singh, F. Muñoz, and A. H. Romero, PyProcar: A Python library for electronic structure pre/post-processing, Comput. Phys. Commun. **251**, 107080 (2020).

[44] See Supplemental Material at http://link.aps.org/supplemental/10.1103/PhysRevB.108.115130 for dynamical and thermal stabilities of XYZ_2 monolayers, band structures of XYZ_2 monolayers, and electronic structures of $SiSnSb_2$ and $GeSnSb_2$ monolayers under external electric field, charge doping, and strain effects.

[45] J. P. Perdew and M. Levy, Physical Content of the Exact Kohn-Sham Orbital Energies: Band Gaps and Derivative Discontinuities, Phys. Rev. Lett. **51**, 1884 (1983).

[46] L. Zhu, T. Zhang, G. Chen, and H. Chen, Huge Rashba-type spin–orbit coupling in binary hexagonal PX nanosheets (X = As, Sb, and Bi), Phys. Chem. Chem. Phys. **20**, 30133 (2018).

[47] D. Domaretskiy, M. Philippi, M. Gibertini, N. Ubrig, I. Gutiérrez-Lezama, and A. F. Morpurgo, Quenching the bandgap of two-dimensional semiconductors with a perpendicular electric field, Nat. Nanotechnol. **17**, 1078 (2022).

[48] Q. Liu, Y. Guo, and A. J. Freeman, Tunable Rashba effect in two-dimensional $LaOBiS_2$ films: Ultrathin candidates for spin field effect transistors, Nano Lett. **13**, 5264 (2013).

[49] D. Di Sante, P. Barone, R. Bertacco, and S. Picozzi, Electric control of the giant Rashba effect in Bulk GeTe, Adv. Mater. **25**, 509 (2013).

[50] C. Yin *et al.*, Tunable surface electron spin splitting with electric double-layer transistors based on InN, Nano Lett. **13**, 2024 (2013).

[51] F. Trier *et al.*, Electric-field control of spin current generation and detection in ferromagnet-free $SrTiO_3$-based nanodevices, Nano Lett. **20**, 395 (2020).

[52] K. Takase, Y. Ashikawa, G. Zhang, K. Tateno, and S. Sasaki, Highly gate-tuneable Rashba spin-orbit interaction in a gate-all-around InAs nanowire metal-oxide-semiconductor field-effect transistor, Sci. Rep. **7**, 930 (2017).

[53] P. Chuang *et al.*, All-electric all-semiconductor spin field-effect transistors, Nat. Nanotechnol. **10**, 35 (2015).

[54] A.-Y. Lu *et al.*, Janus monolayers of transition metal dichalcogenides, Nat. Nanotech. **12**, 744 (2017).

[55] J. Zhang *et al.*, Janus monolayer transition-metal dichalcogenides, ACS Nano **11**, 8192 (2017).

[56] A. Kandemir and H. Sahin, Janus single layers of In_2SSe: A first-principles study, Phys. Rev. B **97**, 155410 (2018).

[57] X. Wu *et al.*, Epitaxial growth and air-stability of monolayer antimonene on $PdTe_2$, Adv. Mater. **29**, 1605407 (2017).

[58] W. Chen *et al.*, Solvothermal synthesis of ternary Cu_2MoS_4 nanosheets: Structural characterization at the atomic level, Small **10**, 4637 (2014).

[59] Y. Lin, S. Chen, K. Zhang, and L. Song, Recent advances of ternary layered Cu_2MX_4 (M = Mo, W; X = S, Se) nanomaterials for photocatalysis, Sol. RRL **3**, 1800320 (2019).